Integrated photonic optomechanical atomic force microscopy probes batch fabricated using deep UV photolithography

D. J. Perez Morelo, M. Wang, V. Madhaven, M. Sathisivan, C. Tay and V. A. Aksyuk

Abstract—**Chip-scale planar nanofabricated optomechanical devices that optically couple a mechanical moving nanostructure to an on-chip photonic cavity of high quality factor can be used for sensing motion with high precision and bandwidth. Motion in nanoscale mechanical structures can be measured optically on-chip with unprecedented precision and bandwidth. Wider scientific and commercial adoption of such sensors required the ability to mass fabricate, flexibility of design, and permanent fiber attachment for robustness and ease of use. In this paper, we demonstrated this by fabricating an atomic force microscopy probe using a commercial foundry process employing deep UV photolithography on 200 mm wafers. The batch fabricated devices with 150 nm minimum features perform similarly to the research prototypes previously fabricated using sequential electron beam lithography. This demonstration eliminates a key technical barrier to the wider adoption of high-performance integrated optomechanical sensing in nanomechanical transducers.**

Index Terms—**cavity optomechanical sensing, integrated photonic**

I. Introduction

MICRO- and nano-optoelectromechanical systems (MOEMS/NOEMS), which enable coupling of optical and mechanical degrees of freedom, have led to many exciting metrology applications including force and displacement measurement [1], [2] torque sensing [3], and the study of vacuum quantum fluctuation at low temperatures [4]. Recently, nanoscale atomic force microscopy (AFM) probes using integrated photonic cavities to achieve high temporal resolution ($<$ 10 ns) and high signal-to-noise ratio (SNR), have been applied for direct measurement of local chemical and thermal properties with nanoscale spatial resolution [5]–[7]. The nanophotonic AFM transducer consists of a curved cantilever probe held in the nearfield of a microdisk optical resonator supporting whispering-gallery modes (WGMs). The demonstration of the full operation of these devices as AFM sensors has previously been reported measurement of local chemical and thermal properties with nanoscale spatial resolution [2], [5]–[9] where different disk-cantilever geometries have been studied. Different photonic AFM probe designs and probe detection schemes have been recently implemented [10]–[14]; for example, a design based on an oscillating ring-shape probe enables remarkably high frequency ($>$100 MHz) operation [11], [12].

Generally, the fabrication of optomechanical devices represents a big challenge, especially if one wants to obtain devices combining small mechanical probe size for fast response and low thermal force noise with good optomechanical coupling and high-optical quality factor (Q_{op}) for sensitive readout [8], [15]. In research settings, such optomechanical integration is typically accomplished by highly customized fabrication processes. For example, nanoscale features and gaps with smooth, vertical sidewalls could be obtained using slow serial electron-beam (e-beam) lithography and carefully tuned inductively coupled plasma reactive ion etching (ICP-RIE). Devices are often fabricated sequentially on small chips with long write times limiting the ability to make long optical waveguides and large-area features for robust optical and mechanical interfaces with conventional single-mode optical fibers used for input and output.Variable Shape Beam (VSB) lithography is an alternative faster e-beam process to fabricate dense repeating pattern in large areas (200 mm wafer scale) with high performance and patterning resolution. Ref. [12] shows that VSB and ICP-RIE processes can be optimized to minimize silicon wall roughness producing high Q_{op} optomechanical devices. Low-cost mass fabrication, flexible selection of chip's size and mechanical form factor, and permanent fiber interfaces are required to extend the application of such integrated chip-scale cavity optomechanical sensors.

Here we demonstrate that fully functional nanophotonic cavity-optomechanical devices with 150 nm critical dimensions can be batch-fabricated on 200 mm wafers using a commercial foundry [16]. The fabrication process included a silicon-on-insulator (SOI) structural layer followed by SiO_2 top cladding and SiN sacrificial etch masking layer. The SOI layer was patterned using 193 nm deep ultraviolet (DUV)

Diego J. Perez-Morelo was with Microsystems and Nanotechnology Division, National Institute of Standards and Technology (NIST), Gaithersburg, MD 20899, USA and Institute for Research in Electronics and Applied Physics, University of Maryland, College Park, MD 20742, USA. He is now with Instituto de Nanociencia y Nanotecnología (INN) Centro Atómico Bariloche, Comisión Nacional de Energía Atómica (CNEA)-CONICET, Argentina (email: diegojavierperez@cnea.gob.ar).

Mingkang Wang is with Microsystems and Nanotechnology Division, National Institute of Standards and Technology (NIST), Gaithersburg, MD 20899, USA and Institute for Research in Electronics and Applied Physics, University of Maryland, College Park, MD 20742, USA. (email: mwangak@connect.ust.hk).

Venkatesh Madhaven, Mogana Sathisivan and Charlie Tay are with SilTerra Malaysia Sdn Bhd, Kedah, MALAYSIA (email: venkatesh_madhaven@silterra.com, mogana_sathisivan@silterra.com, charlie_tay@silterra.com).

Vladimir A. Aksyuk is with Microsystems and Nanotechnology Division, National Institute of Standards and Technology (NIST), Gaithersburg, MD 20899, USA. (email: vladimir.aksyuk@nist.gov).

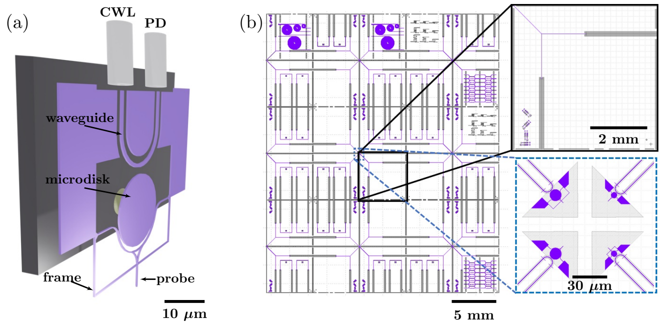

Fig. 1. (a) Schematic of the optomechanical transducer probe consisting of an on-chip waveguide, mechanical probe with a frame, and a microdisk resonator, all made of silicon. A continuous-wave laser (CWL) and a photodetector (PD) are fiber-coupled to the transducer via on-chip optical couplers and waveguide to sense the displacement of the nanoscale cantilever, which is evanescently coupled to microdisk's whispering gallery mode. Optical fibers are not to scale. (b) Mask layout showing 25 mm $\times$ 30 mm pattern containing multiple 5 mm $\times$ 5 mm square individual die (labeled by the black square) with various probe and test devices. The top magnified view shows an individual 5 mm $\times$ 5 mm AFM probe die with two orthogonal fiber V-shaped groove trenches (wider, gray) and Si waveguides (thin gray-purple lines) leading to the device at the corner. The bottom magnified view (dashed blue box) shows four optomechanical AFM probe devices at four adjacent die corners, which are subsequently separated from each other by the die singulation process. Each 25 mm $\times$ 30 mm chip contains 30 optomechanical transducers.

photolithography and etched to define Si device structures, mechanical-released device areas, and the substrate trench areas, which were later used for mechanical chiplet singulation and optical fiber connection. Anisotropic Si substrate etching using cesium hydroxide (CsOH) with high selectivity to oxide was used to define Si V-shaped grooves for fiber attachment and automated mechanical singulation of chiplets with sensors precisely located at chip corners. The released and fiber-pigtailed devices demonstrate high optical quality factor microdisk resonators and high optomechanical coupling for sensitive mechanical motion readout. The ability to expose active photonic and mechanical elements at the chip corner enables multiple mechanical and photonic [12], [17] scanning probe sensing and imaging techniques. This work demonstrates a path for the fabrication of high-performance SOI integrated cavity-optomechanical sensing devices via a combination of commercially available microfabrication processes and widely accessible postprocessing steps.

II. Experimental Method

A. Fabrication of photonic optomechanical probes

The cavity optomechanical devices consist of an optical resonator whose eigenfrequencies are affected by the mechanical motion of the probe [18], [19]. A simple device geometry is shown schematically in Figure 1a, a semicircular cantilever of width w is suspended at its two ends and separated by a nanoscale gap (G) from a nominally 10 μm or 5 μm diameter silicon microdisk. The structures are fabricated from a $\approx$ 220 nm thick silicon layer, and the cantilever has been designed to support a sharp tip at its midpoint. The cantilever has multiple mechanical modes; however, the highest optomechanical coupling to the microdisk resonance is exhibited by the fundamental in-plane mode. We have tested different cantilever

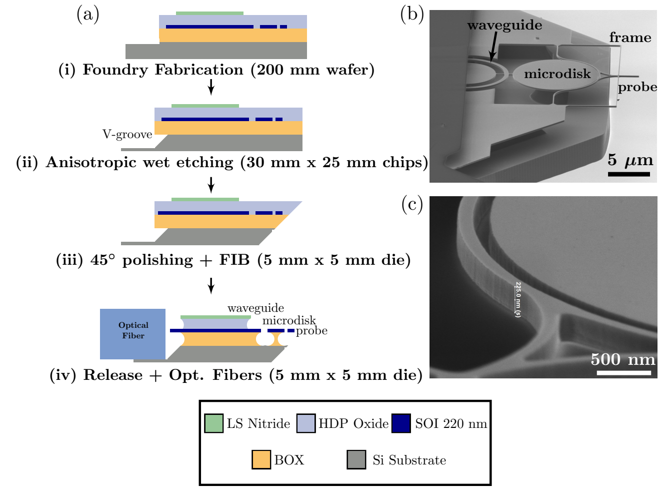

Fig. 2. Device Fabrication. (a) Schematic of fabrication and postprocessing. (i) 200 mm foundry fabricated wafers were diced into 30 mm $\times$ 25 mm chips before further processing. (ii) CsOH anisotropic wet etched V-shaped grooves were used for 5 mm die singulation using the break function of a commercial scribe-and-break tool. (iii) Individual die received $^\circ$ mechanical polishing focused ion beam milling to expose the AFM probe at one corner. (iv) Timed isotropic etch of exposed SiO_2 using 49 % hydrofluoric acid (HF) followed by CO2 critical point drying was used to release mechanical probes. Cleaved bare optical fibers were placed into the $\approx$ 2.5 mm long on-chip V-shaped grooves, actively aligned and glued using a UV curable adhesive. (b) SEM image of a released photonic AFM probe at the chip corner. The waveguide, microdisk and cantilever are visible. A top SiNx layer, as shown in (a), is used to protect the waveguides from HF release. (c) Scanning electron micrograph of a portion of the released SOI probe near the microdisk edge. The actual thickness of the device layer in the SOI is measured to be $\approx$ 225 nm.

designs of varying width w and shape with varying stiffness and typical eigenfrequencies between 2 MHz and 25 MHz.

Figure 1b shows a layout of a 30 mm $\times$ 25 mm optical lithography pattern stepped on the wafer, containing a variety of photonic devices and test structures. It is designed to be singulated into 5 mm $\times$ 5 mm device dies (top inset as an example). The bottom inset shows a magnified view of four adjacent corners of the four separate dies containing AFM probe designs with different disk diameters and probe width and layout.

The process flow used in the nanofabrication of the photonic optomechanical devices is illustrated in Figure 2a. The transducers were fabricated from a nominally 220 nm thick single crystal silicon layer over a 2 μm thick buried oxide (BOX) layer of an SOI chip. Transducers were fabricated on a 200 mm SOI wafer with approximately 40 identical chips of 30 mm $\times$ 25 mm each, containing multiple AFM probe die and a variety of other test structures (see Figure 1b).

The foundry nanofabrication (Fig 2a-i) starts with SOI wafers, and involves multiple noncontact optical lithography/etching/thin film deposition/chemical mechanical polishing (CMP) steps in defining the devices as summarized below: (A) 193 nm optical lithography with a nominal minimum line and space of 120 nm and 100 nm, respectively, is used for defining the devices layer (SOI lithography), followed by Si dry etching. Figure 2c illustrates the typical vertical Si sidewall with low roughness. (B) A layer of $\approx$ 1.7 μm of high-density plasma (HDP) oxide was deposited using chemical vapor deposition (CVD), followed by a planarization step consisting of $\approx$ 0.4 μm CMP and $\approx$ 0.3 μm HDP oxide deposition. A one hour annealing process at 1000 °C was included to densify and improve the film quality of the oxide (cladding layer). (C) Deposition of $\approx$ 300 nm low-stress (LS) silicon nitride (both sides) using low pressure chemical vapor deposition (LPCVD). Second masking step with dry etch is used to open windows in the SiNx on top of the devices, defining fiber coupler structures and V-shaped grooves. Finally, optical lithography followed by a dry etch is used to etch through both oxide layers and stop in the Si substrate for the purpose of creating optical fiber and singulation V-shaped grooves.

B. Postprocessing

The wafers are diced into 30 mm $\times$ 25 mm chips using a dicing saw (see Figure 1b), followed by processing of individual chips. A buffered oxide etch (BOE) 6:1 solution is used for 1 min to remove the silicon native oxide, preparing the substrate surface for a wet etching step. Figure 2a-ii shows the 50 % CsOH anisotropic Si wet etch used to define 80 μm deep V-shaped grooves for optical fibers attachment and die singulation. The $\approx$ 80 μm deep etch was chosen to produce sharp corners for the narrower singulation V-shaped grooves, facilitating mechanical breaking in a scribe-and-break tool (no scribing was used). The wider fiber V-shaped grooves had flat bottoms to reduce the risk of accidental breaks during singulation and handling. The CsOH etch was chosen over other commonly used anisotropic etchants (such as KOH) because it is highly selective for (100) Si not only vs. (111) Si plane, but also vs. silicon dioxide, allowing the $\approx$ 1.3 μm SiO_2 layers to protect the SOI structures during the deep anisotropic Si wet etch [20]. In our design, the transducer features and the inverse-taper optical couplers made in the Si layer are protected by the BOX and the top HDP oxide layers, which are subsequently removed in the HF release.

Angular alignment of the pattern to the crystallographic axis is critical to defining sharp V-shaped grooves and successful singulation. We relied on the notch/flat to crystallographic axis alignment of the commercially purchased SOI wafers and the pattern to notch/flat alignment during patterning and have achieved successful die singulation. Individual 5 mm $\times$ 5 mm die, each containing a single device, are obtained using the alignment and break function of a commercial scribe-and-break tool guided by sharp-bottomed V-shaped groove cleave lines, defined by CsOH etching.

Unlike accelerometer [19], photonic thermometer [21] or other types of potential photonic cavity-based sensors, the application in AFM and photonic probing [22] requires the probe to be located at the device edge to have an unimpeded mechanical or optical access to a sample surface during measurements [6], [23]. It requires additional postprocessing steps. While in the future these can also be performed by batch fabrication at the wafer scale [17], similar to how this is done with traditional AFM cantilevers, for purposes of this research we have post-processed individual device chips (Fig 2a-iii). First, the corner with the transducer was

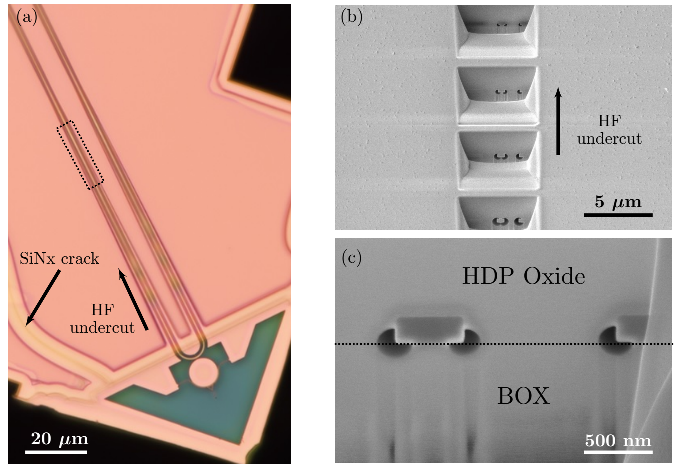

Fig. 3. (a) Optical image of the HF-released optomechanical test device. For testing purposes, the substrate was not removed at this chip's corner. A long undercut along waveguides after 49 % HF silicon dioxide timed etch is evident. HF undercut through a SiNx crack is also visible. Etch time is selected to undercut the oxide under the microdisk away from the WGM optical mode at the disk edge, but such that the oxide remains for mechanical support. (b) SEM image of waveguide cross section corresponding to the dashed rectangular area showed in a. (c) Waveguide zoom-in showing the HF undercut propagating in the bottom corners of the SOI waveguide profile. FIB was used to make the different cross sections.

mechanically polished at 45° from the backside. Thereafter, a focused ion beam (FIB) was used to further undercut the transducer area, exposing the AFM probe tip at the chip corner and to further sharpen the tip (see Figure 2b). Finally, the devices are released by wet etching in an HF water solution (49 % mass fraction), followed by sequential rinsing in water and isopropyl alcohol and supercritical point drying (Fig 2a-iv). For other cavity optomechanical devices where additional postprocessing to expose the device at the chip corner is not needed, we anticipate that the sacrificial oxide wet etch can be performed after the CsOH V-shaped groove etch and before device singulation into individual die. Both wet etch steps may in principle be performed at wafer scale.

During the post processing and device characterization we faced some issues, such as cracks on the top silicon nitride and acid over-etching during the release step, both illustrated in Figure 3. We observed that silicon nitride layer deposited on HDP oxide by LPCVD exhibits large tensile stress ($\approx$ 1200 MPa), which may cause visible corner cracking during the chip dicing and dice singulation steps. If any cracks eventually go through the top part of a waveguide, the HF undercut through the crack (during the release step) is going to affect the waveguide oxide support. This may increase the optical losses, affecting the performance of the devices. Lower stress nitride layers were obtained when the fabrication process was modified to include silicon-rich LPCVD nitride (tensile stress $\approx$ 400 MPa). Since light is tightly confined within the high index Si waveguide, with the $\approx$ 1.6 μm thick top oxide cladding used here, simulations and previous measurements suggest that the waveguide optical propagation losses across the 5 mm chips are not measurably affected by the SiN optical properties, such as any possible absorption differences between stochiometric and Si-rich composition. The SiN is not present above the microdisk resonator.

Additionally, we found that HF propagates and etches quickly along a bottom corner of the patterned SOI layer/BOX interface, attributed to a keyhole or weak seam, most likely induced during the Si structure formation. The defect is not visible in the cross sections without the HF etch but is clearly visible after HF dip (see Figure 3b and 3c). This problem is attributed to the nanoscale unfilled void at the bottom corner of the Si wall, which is not able to be filled by HDP oxide deposition. The void formation is attributed to a slight undercut of the SOI BOX layer during post-Si-etch cleaning. This resulting nanochannel is attacked and widened by HF during the release process allowing it to penetrate tens of microns deep along the sidewall corner. The symmetric cross-section of the channel shows that the HDP oxide is about as dense as the BOX on the bottom, as they are being etched by HF at the same rate. A similar problem has been reported by Michels et al. [20] previously in photonic AFM probe fabrication. Much shorter or no undercut was observed in the devices after the foundry fabrication process was modified by removing a dilute HF in the post-Si-etch clean after SOI etching. While strongly reducing the formation of the undercut holes along the waveguides during the release, elimination of the HF clean step after the Si etch did not seem to have any detectable negative effects. Here we note that we did not perform careful propagation loss measurements on the waveguides to distinguish such losses from the coupling losses to single-mode fibers via the inverse tapers.

III. RESULTS AND DISCUSSION

For testing the performance of the device, we glued the optical fiber to the chip using the fabricated V-shaped groove as we described in the previous section. First, we use a micropositioner for fiber alignment while we measure the light transmission using the setup shown schematically in Figure 4a. A small drop of UV curable adhesive was placed in each V-shaped groove. The optical fibers were placed in the V-shaped grooves and manipulated by the micropositioners until the optical transmission was maximized. The adhesive was UV cured for the first fiber and the gluing process was repeated for the second fiber. We measured the batch fabricated devices using a 1550 nm band tunable diode laser attenuated and coupled into the device using optical fibers. Figure 4b shows the WGM resonances in the transmission spectrum as a function of the laser wavelength. The light is evanescently coupled from the waveguide to the Si microdisk. While the disk supports transverse electric (TE) and transverse magnetic (TM) polarized WGMs, the input polarization was adjusted and integrated waveguide separation was optimized for coupling to TMn,m modes [8], [9], identified by their free spectral range (FSR, spacing between modes) which are $\approx$ 15 nm and $\approx$ 14 nm for two groups of modes in the 10 μm diameter disks. The measurement is consistent with numerical modeling. The spectrum shows a gradual intensity drop starting at $\approx$ 1510 nm, which is attributed to the radiation loss cutoff for the waveguide loop at the coupling point (see Figure 2b). It is important to mention that the same background is observed in the waveguide transmission without the microdisk resonator.

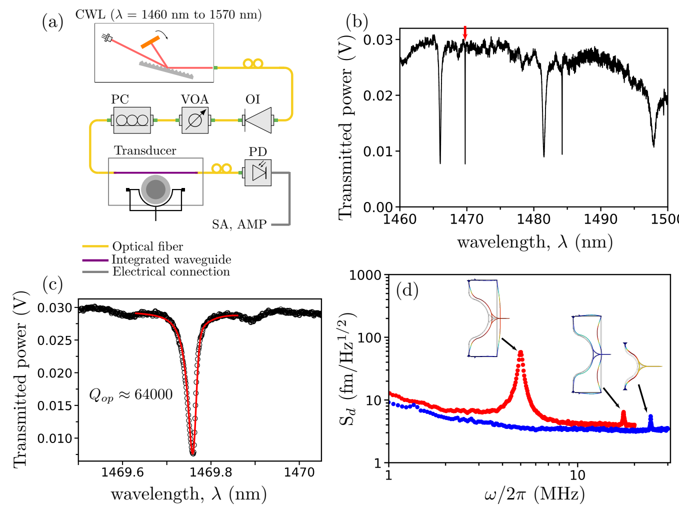

Fig. 4. Measuring photonic optomechanical devices: (a) Schematic of full experimental setup for device characterization, containing a continuous-wavelength tunable diode laser (CWL), optical isolator (OI), variable optical attenuator (VOA), polarization controller (PC), electronic amplifier (AMP), Spectrum analyzer (SA) and photodetector (PD). (b) Broad wavelength scan for transverse magnetic (TM) polarized modes of a typical disk-cantilever device ($w = 150$ nm, $G = 180$ nm) (c) High-Q optical resonance indicated with an red arrow in (b), (d) Transducer non-contact noise spectral density, S_d, for two devices with different dimensions. Device with a 10 μm disk (upper, red) presents a lowest in-plane mode eigenfrequency of $\omega_0/2\pi \approx$ 5 MHz and damping coefficient $\Gamma/2\pi \approx$ 0.34 MHz while the 5 μm disk device (lower, blue) presents $\omega_0/2\pi \approx$ 25 MHz and damping coefficient $\Gamma/2\pi \approx$ 0.28 MHz. The modal shapes for in-plane modes, obtained from finite-element-method (FEM) simulations, are shown in the insets.

TABLE I
RELEVANT PARAMETERS OF THE DEVICES FOR DUV AND E-BEAM LITHOGRAPHY

Lithography	Q_{op}	$g_{OM}/2\pi$ (GHz/nm)	FSR (nm)
DUV*	$\approx 6.4\times10^4$	≈ 5.3	14, 15
E-beam**	$\approx 1\times10^5$	≈ 0.5	14.7, 15.3 and 16.4

*10 μm disk optomechanical device, 220 nm thick SOI, this work.
**10 μm disk optomechanical device, 260 nm thick SOI, Ref. [7]–[9].

The transmission signal corresponding to an individual resonance is shown in Figure 4c, presenting an $\lambda = 1469.76$ nm and an optical quality factor of $Q_{op} \approx 64000$. A comparison of the relevant parameters for similar devices fabricated using e-beam lithography and ICP-RIE are shown in Table I. We noted that devices fabricated using 220 nm thick SOI exhibit a notably larger optomechanical coupling g_{OM} compared with the other optomechanical AFM probes [7]–[9]. Based on the spectral measurements and simulations the thinner disk is close to the mode confinement cutoff at the wavelength used, and we think this leads to a stronger evanescent interaction with the cantilever.

Finally, Figure 4d shows the power spectral density calibrated from the integrated voltage noise power and the equipartition theorem [6], [24]. Fitting a Lorentzian function to the thermal noise spectrum yields a mechanical eigenfrequency of $\omega_0/2\pi \approx$ 5 MHz and damping coefficient $\Gamma/2\pi \approx$ 0.34 MHz. The high dissipation rate of the mechanical mode is dominated by the viscous damping from the air environment.

The FEM-simulated mechanical in-plane mode shapes are also included in the Figure.

AFM photonic devices with 5 μm disk with different cantilever designs were also tested showing mechanical response of the cantilever with a fundamental in-plane mode at $\omega_0/2\pi \approx 25$ MHz and damping coefficient $\Gamma/2\pi \approx 0.28$ MHz (See Figure 4d).

IV. Conclusion

In summary, we demonstrate a MHz-bandwidth photonic AFM optomechanical probe fabricated in a commercial semiconductor foundry. The device presents sensitive transduction of motion of a nanoscale cantilever in the range of a few femtometers per root-hertz using a high-quality factor microdisk optical resonator $\approx$ 64000, both foundry-fabricated using high resolution optical lithography. This approach opens the doors for microfabricating a variety of useful photonic sensors such as thermometers, accelerometers, and gyroscopes. Future works will be aimed at testing different AFM photonic probe designs in experimental setups such as photothermal-induced resonance (PTIR) spectroscopic technique where the low-drag cross-section of these transducers open new opportunities for nanoscale chemical and thermal imaging.

Acknowledgments

D.J.P. and M.W. were supported by the Cooperative Research Agreement between the University of Maryland and the National Institute of Standards and Technology Center for Nanoscale Science and Technology, Award 70NANB14H209, through the University of Maryland. Research performed in part at the National Institute of Standards and Technology Center for Nanoscale Science and Technology.

Data availability Data presented in this paper is available at the NIST public data repository doi:10.18434/mds2-2815.

References

[1] G. Anetsberger et al., "Measuring nanomechanical motion with an imprecision below standard quantum limit" *Phys. Rev. A*, vol. 82, pp. 061804(4), 2010. doi: 10.1103/PhysRevA.82.061804

[2] K. Srinivasan, H. Miao, M. T. Rakher, M. Davanco and V. Aksyuk, "Optomechanical Transduction of an Integrated Silicon Cantilever Probe Using a Microdisk Resonator" *Nano Lett.*, vol. 11, pp. 791-797, 2011. doi: 10.1021/nl104018r

[3] Wu, M. et al., "Dissipative and dispersive optomechanics in a nanocavity torque sensor" *Phys. Rev. X*, vol. 4, pp. 021052(11), 2014. doi: 10.1103/PhysRevX.4.021052

[4] Norte, R.A., Forsch, M., Wallucks, A., Marinkovic, I., and Groblacher, S., "Platform for Measurements of the Casimir Force between Two Superconductors" *Phys. Rev. Lett.*, vol. 121, pp. 030405(6), 2018. doi:10.1103/PhysRevLett.121.030405

[5] An, S. M. et al., "Optomechanical transducer-based soft and high frequency nanoscale cantilever for atomic force microscopy" *In Proceedings, Solid State Sensor, Actuator and Microsystems Workshop, Hilton Head Island, SC*, June 5-9, pp. 266-269 2016. doi: 10.31438/trf.hh2016.71

[6] J. Chae et al., "Nanophotonic Atomic Force Microscope Transducers Enable Chemical Composition and Thermal Conductivity Measurements at the Nanoscale" *Nano Lett.*, vol. 17, pp. 5587-5594, 2017. doi: 10.1021/acs.nanolett.7b02404

[7] M. Wang, G. Ramer, D. J. Perez-Morelo, G. Pavlidis, J. J. Schwartz, L. Yu, R. Ilic, V. A. Aksyuk and A. Centrone, "High throughput, high accuracy nanoimaging of thermal conductivity and interfacial thermal conductance" *Nano Lett.*, vol. 22, 11 pp. 4325-4332, 2022. doi: 10.1021/acs.nanolett.2c00337

[8] M. Wang, D. J. Perez-Morelo and V. Aksyuk, "Using thermo-optical nonlinearity to robustly separate absorption and radiation losses in nanophotonic resonators" *Optics Express*, vol. 29, 5, pp. 6967-6979 2022. doi: 10.1364/OE.416576

[9] M. Wang, D. J. Perez-Morelo and V. Aksyuk, "Overcoming thermo-optical dynamics in broadband nanophotonic sensing" *Microsyst Nanoeng*, vol. 7, 52, pp. 1-11 2021. doi: 10.1038/s41378-021-00281-y

[10] M. Zawierta, et al., "Atomic force microscopy with integrated on-chip interferometric readout " *Ultramicroscopy*, vol. 205, pp. 75-83, 2019. doi: 10.1016/j.ultramic.2019.05.011

[11] P. E. Allain et al., "Optomechanical resonating probe for very high frequency sensing of atomic forces" *Nanoscale*, vol. 12, pp. 2939-2945, 2020. doi: 10.1039/C9NR09690F

[12] L. Schwab, P. E. Allain , N. Mauran , X. Dollat , L. Mazenq, D. Lagrange, M. Gély, S. Hentz, G. Jourdan , I. Favero and B. Legrand, "Very-high-frequency probes for atomic force microscopy with silicon optomechanics" *Microsyst Nanoeng*, vol. 8, 32 , pp. 1-14 , 2022. doi: 10.1038/s41378-022-00364-4.

[13] F. He, J. Liu and K. Zhu., "Optomechanical atomic force microscope" *Nanotechnology*, vol. 32, pp. 085505(7), 2021. doi: 10.1088/1361-6528/abc711

[14] F. Galeotti et al., "Demonstration of atomic force microscopy imaging using an integrated opto-electro-mechanical transducer" *Ultramicroscopy*, vol. 230, pp. 113368, 2021. doi: 10.1016/j.ultramic.2021.113368

[15] M. W. Pruessner et al., "Foundry-processed optomechanical photonic integrated circuits" *OSA Continuum*, vol. 4, pp. 1215-1222, 2021. doi: 10.1364/OSAC.419410

[16] General fabrication capabilities are described here: https://www.silterra.com/technology/technology#section07. The full description of the procedures used in this paper requires the identification of certain commercial services and their suppliers. The inclusion of such information should in no way be construed as indicating that such services or suppliers are endorsed by NIST or are recommended by NIST or that they are necessarily the best services or suppliers for the purposes described.

[17] T. Michels, I. W. Rangelow, V. A. Aksyuk, "Fabrication process for an optomechanical transducer platform with integrated actuation" *J. Res. Natl. Inst. Stand.*, vol. 121, pp. 507-536, 2016. doi: 10.6028/jres.121.028

[18] G. Anetsberger, O. Arcizet, Q. Unterreithmeier, et al., "Near-field cavity optomechanics with nanomechanical oscillators" *Nature Phys*, vol. 5, pp. 909-9014, 2009. doi: 10.1038/nphys1425

[19] A. G. Krause, M. Winger, T. D. Blasius, Q. Lin and O. Painter, "A high-resolution microchip optomechanical accelerometer" *Nature Photon*, vol. 6, pp. 768-772, 2012. doi: 10.1038/nphoton.2012.245

[20] F. A. Chambers and L. S. Wilkiel, "Cesium hydroxide etching of (100) silicon (for optical fiber attachment)" *J. Micromech. Microeng.*, vol. 3, pp.1, 1993. doi: 10.1088/0960-1317/3/1/001

[21] N N. Klimov and Z. Ahmed, "Fabrication and Testing of Photonic Thermometers" *J Vis Exp.*, vol. 140, pp. 55807(5), 2018. doi: 10.3791/55807

[22] T. Michels and V. Aksyuk, "Optical Probe for Nondestructive Wafer-Scale Characterization of Photonic Elements" *IEEE Photonics Technology Letters*, vol. 29, 8 pp.643-646, 2017. doi: 10.1109/LPT.2017.2660439

[23] S. An, T. Michels, J. Zou, D. A. Westly, and V. A. Aksyuk, "Optomechanical transducer-based nanocantilever for atomic force microscopy" *nternational Conference on Optical MEMS and Nanophotonics (OMN)*, pp. 1-2, 2015. doi: 10.1109/OMN.2015.7288864.

[24] B.D. Hauer, C. Doolin, K.S.D. Beach, J.P. Davis, "A general procedure for thermomechanical calibration of nano/micro-mechanical resonators" *Annals of Physics*, vol. 339, pp. 181-207, 2013. doi: 10.1016/j.aop.2013.08.003